

Planetesimal gravitational collapse in gaseous environment: thermal and dynamic evolution

P. Segretain¹, H. Méheut¹, M. Moreira², G. Lesur³, C. Robert³, and J. Mauxion³

¹ Université Côte d'Azur, Observatoire de la Côte d'Azur, CNRS, Laboratoire Lagrange, Bd de l'Observatoire, CS 34229, 06304 Nice cedex 4, France e-mail: paul.segretain@oca.eu

² ISTO, Institut des Sciences de la Terre d'Orléans, 45071 Orléans, France

³ Univ. Grenoble Alpes, CNRS, IPAG, 38000 Grenoble, France

Received XX Accepted YY

ABSTRACT

Planetesimal formation models often invoke gravitational collapse of pebble clouds to overcome various barriers to grain growth and propose processes to concentrate particles sufficiently to trigger this collapse. On the other hand, the geochemical approach to planet formation constrains the conditions for planetesimal formation and evolution by providing temperatures that should be reached to explain the final composition of planetesimals, the building blocks of planets. To elucidate the thermal evolution during gravitational collapse, we use numerical simulations of a self-gravitating cloud of particles and gas coupled by gas drag. Our goal is to determine how the gravitational energy relaxed during the contraction is distributed among the different energy components of the system, and how this constrains the thermal and dynamical planetesimals' history. We identify the conditions necessary to achieve a temperature increase of several hundred Kelvins, potentially reaching up to 1600 K. Our results emphasize the key role of the gas during the collapse.

Key words. Planet formation - Gravitational collapse - Planetesimals - Thermal histories

1. Introduction

The formation of planetesimals is one of the key open questions in planet formation. Not only is it necessary to identify the properties of the building blocks of planets but determining the physical conditions experienced during the formation of parent bodies could also benefit the understanding of the chemical and isotopic composition of small bodies of the Solar System and meteorites (Boyett et al. 2018; Zhu et al. 2023). These gravitationally bound objects have a size of 1 – 1000 km and a common view is that their destructive collision cascade is at the origin of the asteroid and Kuiper belts as well as the Oort cloud in the Solar System (Morbidelli & Nesvorný 2020), whereas protoplanets are the result of their constructive collisions and growth (Johansen & Lambrechts 2017). Indeed, both the isotopic chronology of meteorites, which are fragments of asteroids and the detection of protoplanets within gaseous protoplanetary discs (Keppler et al. 2018; Gratton et al. 2019) suggest that planetesimals form during the first Myr of the stellar system, in the gaseous protoplanetary disc era (Kruijer et al. 2014).

However, the pebble-sized bodies from which planetesimals arise drift radially through the disc towards the star on very short timescales of hundreds to thousands of years due to the gas drag (Weidenschilling 1977) while the bouncing, erosion or fragmentation barriers could severely limit their growth (Blum 2018). Recently, simulations of dust aggregates of sub-micrometre monomers show that their growth by collisions could allow to overcome the fragmentation barrier. (see e.g. Hasegawa et al. 2021, 2023). In this model Kobayashi & Tanaka (2021, 2023) show that pebbles could form planetesimals and then gas giant planets in a relatively short time. Another path to overcome these barriers and form planetesimals commonly considered invokes a

strong concentration of grains, followed by a gravitational collapse on a short timescale. The physical processes responsible for the strong clustering of solids are currently under debate, including in particular the streaming instability (e.g. Youdin & Goodman 2005; Carrera & Simon 2022), the concentration in magneto-rotational instability zonal flows (e.g. Fromang & Nelson 2006; Johansen et al. 2011; Dittrich et al. 2013) but also instabilities forming vortices such as the Rossby wave instability (e.g. Lovelace et al. 1999; Meheut et al. 2012), the vertical shear instability (e.g. Urpin & Brandenburg 1998; Nelson et al. 2013; Manger & Klahr 2018) or the convective over-stability (e.g. Klahr & Hubbard 2014; Lyra 2014; Raettig et al. 2021), as well as turbulent clustering (e.g. Cuzzi et al. 2001; Pan et al. 2011; Gerosa et al. 2023). In most of the works cited above, only one or a small number of sizes were considered for the solids. The efficiency of these different mechanisms when considering a realistic size distribution is a point of debate. For example, in the case of streaming instability, Krapp et al. (2019) claimed that including a particle size distribution could greatly reduce the instability growth time, while Schaffer et al. (2021) found that dust size distribution changes the dynamics but does not suppress strong clustering. All of these clustering processes rely on a balanced coupling between the gas and the solid phase: the solid has to follow but only partially the gas dynamics, and possibly modify this gas dynamics as in the streaming instability. This means that the solid Stokes number generally lies in the range $[10^{-2}; 1]$ where the Stokes number St quantifies the ratio between the stopping time, the typical timescale required for the solid velocity to reach the gas velocity, and the typical timescale of the gas dynamics, which is generally the orbital period (see e.g. Lesur et al. 2023).

The following step, the gravitational collapse, is key to characterizing the properties of planetesimals and has been investigated in several ways. The results of collisions on the final grain sizes in the planetesimal were investigated by Wahlberg Jansson et al. (2017) and how the initial angular momentum of the particle cloud is responsible for the binary nature of planetesimals by Nesvorný et al. (2021). More recently, Lorek & Johansen (2024) evaluated how the initial rotation of a pebble cloud modifies the final shape of the planetesimal formed. All of these studies focused on the dynamics of the solids without considering the gas. This is consistent with the high dust-to-gas ratio and the location considered, in the outer solar system, where the gas density is lower and the stopping time is therefore longer than the collision time. In fact, as the particles that tend to cluster have Stokes number in the range $[10^{-2}; 1]$, the coupling with the gas may also have non-negligible effects during the collapse. Polak & Klahr (2023) built on the work by Nesvorný et al. (2021) and studied the impact of the initial location of the collapsing clump on the number and size distribution of the formed planetesimals. Wahlberg Jansson & Johansen (2017) added the gas drag in the dynamics of solids and showed how it modifies the structure of the formed object, with medium-sized pebbles at the centre surrounded by a mixture of large and small pebbles. Shariff & Cuzzi (2015) examined the two-way coupling between gas and solids during the contraction and observed an oscillatory behaviour of the pebble clump. As they point out, for a minimum-mass solar nebula given by Hayashi (1981), this oscillatory behaviour requires very large and dense clumps, for which no formation process is known. Moreover, these results focus on the isothermal case, where no gas heating process is included. To pave the way towards an understanding of planetesimal formation that is consistent with both the disc gas-dust dynamics and the cosmochemical constraints from the Solar System, we consider here the gas dynamical and thermal evolution during the collapse. As we show below, this approach is particularly important for AU-scale planetesimal formation.

In this paper we consider a gravitational collapse of pebbles, modifying the gas dynamics and temperature. We build on the work of Shariff & Cuzzi (2015), considering a spherically symmetric collapse, where we take into account the gas thermodynamics and include the frictional heating of the dust on the gas. The paper is structured as follows. In section 2, we discuss paths to model the collapse of a dust clump coupled to a gaseous environment and introduce some necessary physical concepts. The numerical methods are presented in section 3, and we discuss the results and their limits in section 5.

2. Model for pebbles collapse in a fluid

In this study, we assume a spherical pebble cloud collapsing under self-gravity in a gaseous environment. Given the length scales that will be involved in this work, small compared to disc pressure length scales, the gas Keplerian shear and disc rotation are neglected. The exact background gas velocity profile varies with the particle clustering process (in a vortex, in a pressure bump, ...), and we here consider the simple case with no initial velocity in the referential centred on the pebble cloud centre. In this section, we present some characteristic times, and the governing equations for gas and solid evolution, before giving a first simple analytical estimate of the gas temperature increase during the collapse.

2.1. Characteristic times

The gravitational collapse of a coupled pebble and gas cloud involves several timescales. The disc dynamical timescale is the Keplerian orbital time, $t_{\text{orb}} = 2\pi\sqrt{a^3/\mathcal{G}M_{\odot}}$ where \mathcal{G} is the gravitational constant, a the semi-major axis of the orbit and M_{\odot} the central star mass. We consider in this work gravitational collapses occurring in the inner disc typically at 1 AU (or less) from the central star. At such a distance, around a solar-type star, $t_{\text{orb}} \sim 1$ yr.

We study a spherical clump with a mass M and initial radius R_0 composed of gas and particles. The position of a particle located at the cloud surface evolves under the clump gravity and the gas drag which is expected to be linear in the inner part of discs and follows the equation

$$\frac{d^2r}{dt^2} = -\frac{\mathcal{G}M}{r^2} - \frac{1}{\tau_s} \frac{dr}{dt}, \quad (1)$$

with τ_s the particle friction time or stopping time, and where the gas is assumed static. To obtain a first rough estimation, we consider the terminal velocity approximation. In this approximation ($d_t^2 r \sim 0$), eq. 1 gives

$$r(t) = \sqrt[3]{R_0^3 - 3\tau_s \mathcal{G}M t}. \quad (2)$$

and the collapse time (when $r = 0$) is

$$t_{\text{col}} = \frac{R_0^3}{3\mathcal{G}M\tau_s} = \frac{8t_{\text{ff}}^2}{3\pi^2\tau_s} = \frac{8t_{\text{ff}}}{3\pi^2\text{St}_{\text{ff}}}, \quad (3)$$

with the free-fall time defined as

$$t_{\text{ff}} = \frac{\pi}{2} \sqrt{\frac{R_0^3}{2\mathcal{G}M}}$$

. We have introduced the Stokes number for this dynamical evolution $\text{St}_{\text{ff}} = \tau_s/t_{\text{ff}}$. This differs from the standard Stokes number used for protoplanetary discs $\text{St}_{\Omega} = \tau_s\Omega = 2\pi\tau_s/t_{\text{orb}}$. Equation 3 shows in particular that the pebble collapse time is inversely proportional to the Stokes number St_{ff} .

In Fig. 1 the time evolution of the clump size estimated in the terminal velocity approximation (equation 2) is compared with the numerical solution of equation 1 with a static gas, and with a hydrodynamical simulation (fiducial case, see section 3.1). The cloud size is characterized by its mean radius, defined as in (Shariff & Cuzzi 2015)

$$r_m = \frac{\int_0^{+\infty} r\rho_p(r)dr}{\int_0^{+\infty} \rho_p(r)dr}.$$

For a filled sphere of uniform density and radius R_0 , the value of r_m is $0.5R_0$. Figure 1 shows that the terminal velocity approximation (eq. 3) underestimates by about 10% the collapse time when compared with hydrodynamical simulations. t_{col} (here about 6.10^6 s) is, therefore, a good proxy for the collapse time. Moreover, the static gas solution matches very well with the numerical simulation. It thus provides an upper limit for the simulation integration time.

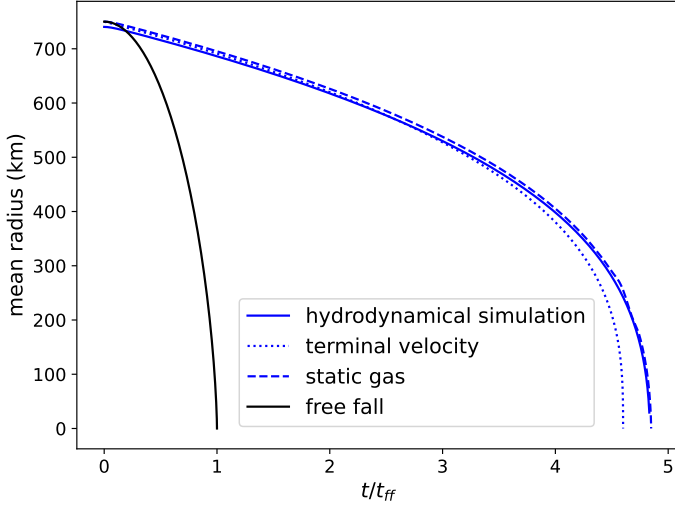


Fig. 1: Time evolution of the pebble cloud size in the non-linear numerical simulation, a static gas solution (Eq. 1), and the analytical solution 2 in the terminal velocity approximation (respectively solid, dashed and dotted line). The black line corresponds to the standard free fall, without friction (see appendix A.1).

2.2. Governing equations

The gas dynamics is given by the inviscid Euler equations

$$\partial_t \rho_g + \nabla \cdot (\rho_g \mathbf{u}) = 0 \quad (4)$$

$$\partial_t \rho_g \mathbf{u} + \nabla \cdot (\rho_g \mathbf{u} \otimes \mathbf{u} + P) = -\rho_g \nabla (\phi_{g+p} + \phi_c) - \rho_p \mathbf{a}_{\text{drag}} \quad (5)$$

$$\partial_t E + \nabla \cdot (\mathbf{u}(E + P)) = -\rho_g \mathbf{u} \cdot \nabla (\phi_{g+p} + \phi_c) + \mathcal{P}_{\text{drag}} \quad (6)$$

where ρ_g , \mathbf{u} , P and E are respectively the mass density, the velocity, the pressure and the total energy (kinetic and internal) of the gas. We consider the self-gravity of the gas and dust, and the drag force between them. In the momentum equation, ρ_p is the local pebble mass density. The equation system is closed with an ideal equation of states written as

$$P = \rho_g \frac{R}{M} T, \quad U = \frac{P}{\gamma - 1} \quad (7)$$

where R , M , T , U and γ are the ideal gas constant, the molar mass, the temperature, the internal energy and the adiabatic index of the gas.

Pebbles are modelled as a pressure-less fluid whose dynamic is given by

$$\partial_t \rho_d + \nabla \cdot (\rho_d \mathbf{v}_d) = 0 \quad (8)$$

$$\partial_t \rho_d \mathbf{v}_d + \nabla \cdot (\rho_d \mathbf{v}_d \otimes \mathbf{v}_d) = -\rho_d \nabla (\phi_{g+p} + \phi_c) + \rho_d \mathbf{a}_{\text{drag}} \quad (9)$$

where ρ_d and \mathbf{v}_d are the mass density and the velocity of the fluid. ϕ_{g+p} is the gravitational potential of both gas and pebbles, which solves the Poisson equation

$$\Delta \phi_{g+p} = 4\pi G \rho_{g+p} \quad (10)$$

where ρ_{g+p} is the total mass density of gas and pebbles. ϕ_c is addressed in section 3 where its introduction is justified by the limited simulation domain.

In these equations, \mathbf{a}_{drag} is the drag acceleration exerted by the gas on pebbles (and $-\mathbf{a}_{\text{drag}}$ the feedback onto the gas). The drag acceleration is computed with the prescription

$$\mathbf{a}_{\text{drag}} = -\frac{\mathbf{v}_d - \mathbf{u}}{\tau_s} \quad (11)$$

where τ_s is the dust stopping time given by

$$\tau_s = \begin{cases} \frac{\rho_m a}{\rho_g \bar{c}} & \text{if } a < 9\lambda/4 \text{ (Epstein regime, Epstein 1924)} \\ \frac{4\rho_m a^2}{9\rho_g \bar{c} \lambda} & \text{else (Stokes regime)} \end{cases} \quad (12)$$

depending on the material density ρ_m and size a of the pebbles, the density ρ_g of the gas and the mean thermal speed of the gas molecules $\bar{c} = \sqrt{8/\pi} c_s$, with c_s the sound speed in the gas. λ is the mean-free path of the gas molecules. In the energy equation, $\mathcal{P}_{\text{drag}}$ is the power given by the particles to the gas, defined as

$$\mathcal{P}_{\text{drag}} = \rho_p \frac{\mathbf{v}_p - \mathbf{u}}{\tau_s} \cdot \mathbf{u} + \rho_p \frac{(\mathbf{v}_p - \mathbf{u})^2}{\tau_s}. \quad (13)$$

This includes the power done by the drag force and the frictional heating which can be considered as irreversible power generating entropy.

Finally, in the collapsing area, the pebbles are highly concentrated compared to the disc mean solid density, it can be considered as regions with a large concentration of dust of many sizes (not included in the simulations) and therefore optically thick. We then consider an adiabatic evolution for the system of gas and pebbles.

2.3. Static gas

An estimation of the heating by gravitational collapse could be provided assuming here a static gas and using an energetic approach where the initial gravitational energy of the pebbles would be fully converted into gas internal energy. This would mean that the pebbles fully transfer their kinetic energy to gas through friction. This simple approach mimics some estimations made to obtain an upper limit on the temperature of a geophysical body (see e.g. Lichtenberg et al. 2023, section 2.1.1).

The initial condition is a spherical pebble cloud with a uniform mass density¹. The gravitational energy of the ball of mass M and initial radius R_0 , is $E_G = -3GM^2/5R_0$. An infinitesimal contraction of the pebble ball releases the gravitational energy

$$dE_G = \frac{3}{5} \frac{GM^2}{R^2} dR. \quad (14)$$

Assuming this released gravitational energy spread uniformly in the ball of the same radius R , the gas temperature would increase by this infinitesimal contraction by

$$dT = \left(\frac{c_v}{V_m} \frac{4}{3} \pi R^3 \right)^{-1} dE_p = \frac{9GM^2}{20\pi c_v V_m} \frac{dR}{R^5}, \quad (15)$$

with c_v the molar heat capacity at constant volume and V_m the molar volume. The gas shell of radius \tilde{R} receive energy from the solids through drag only when the pebble cloud is larger than \tilde{R} . The temperature at a radius \tilde{R} would have increased by the end of the collapse of

$$\Delta T(\tilde{R}) = \int_{\tilde{R}}^{R_0} \frac{dT}{dr} dr = \frac{9GM^2}{20\pi c_v V_m} \frac{1}{4} \left(\frac{1}{\tilde{R}^4} - \frac{1}{R_0^4} \right). \quad (16)$$

For a pebble cloud of mass 3×10^{16} kg contracting from $R_0 = 1500$ km to $\tilde{R} = 50$ km, the gravitational energy released is

¹ We define here a *ball* as a filled sphere or a solid sphere, and a *sphere* as the surface of a ball

$\Delta E_{\mathcal{G}} = 3\mathcal{G}M^2/5 \times (1/\tilde{R} - 1/R_0) \sim 7 \times 10^{17}$ J. If this energy is deposited through the process described above in a gas initially at 320 K and 8.34 Pa composed fully of H_2 , (which corresponds to a total mass of about 9×10^{13} kg, and $c_v = 20.8 \text{ J} \cdot \text{mol}^{-1} \cdot \text{K}^{-1}$) the temperature would reach more than 5000 K according to equation 16.

This simple approach gives an upper limit to gas heating. The very high temperature obtained here shows that the hypothesis of a full conversion of gravitational energy into gas internal energy is not correct. Therefore a more complete approach, including the gas and dust thermal as well as dynamical evolution with fully non-linear numerical simulations is necessary.

3. Numerical methods

We perform 1D spherically symmetric simulations using the IDEFIX code (Lesur et al. 2023), solving the hydrodynamical equations with finite-volume methods through a Godunov scheme. IDEFIX also includes a self-gravity module (Mauxion et al. 2024, appendix A) to solve the Poisson equation with linear algebra methods. The solids can be modelled in two ways. In this paper, we choose to model them as a pressure-less fluid. We provide a comparison with a Lagrangian particle model in appendix C, showing that for our problem the two approaches are similar. The runs have been performed using a second-order Runge-Kutta scheme, second-order spatial reconstruction and the Lax-Friedrichs Riemann solver.

3.1. Initial conditions

Initially, the pebbles are static, forming a clump with a uniform density profile in the core and a Gaussian outer profile decrease:

$$\rho_p(r) = \begin{cases} \rho_c & \text{if } r \leq r_c \\ \rho_c \exp\left(-\frac{(r-r_c)^2}{\sigma^2}\right) & \text{elsewhere} \end{cases} \quad (17)$$

r_c is the initial core radius of the clump, and we define the initial radius of the pebble sphere as $R_0 = r_c + \sigma$ with $\sigma = r_c/5$. The gas has no initial velocity, a uniform density ρ_0 and temperature T_g with an ideal equation of state. The adiabatic index of the gas is 1.4. The initial stopping time τ_p is 8.4×10^4 s corresponding (for the chosen gas density and sound speed) to pebbles with $a = 15$ cm and $\rho_m = 3 \text{ g} \cdot \text{cm}^{-3}$, and to $\text{St}_{\text{ff}} = 0.06$. For these pebbles, the stopping time is computed in the Stokes regime.

Our fiducial simulation have a pebble mass M_{fid} of 3×10^{16} kg and gas density ρ_{fid} of $7 \times 10^{-6} \text{ kg} \cdot \text{m}^{-3}$. This fiducial mass corresponds to a core density ρ_c of $2.1 \times 10^{-3} \text{ kg} \cdot \text{m}^{-3}$ in equation 17, and thus to an initial dust-to-gas ratio of 300. We explore how the total pebble mass M_{tot} and initial gas density ρ_g modify the final temperature. The values employed for the various runs are presented in table 1. Assuming a planetesimal density of $2000 \text{ kg} \cdot \text{m}^{-3}$ (which would correspond to planetesimals made of silicates with some porosity), these initial masses

Parameter	Value
M_{tot}	{1; 1.7; 2.3; 3.3; 5} M_{fid}
ρ_g	{0.5; 0.7; 1; 1.4; 2.1; 3} ρ_{fid}
a	{5; 10; 15; 20} cm
ρ_m	{1; 3; 5; 7} $\text{g} \cdot \text{cm}^{-3}$

Table 1: Range of values used for our runs.

correspond to spherical planetesimals with radii between 10.6 and 26.1 km. The initial size and mass of our pebble cloud are therefore small compared to the characteristic size of the parent bodies of the current main belt asteroids. The initial gas temperature (320 K) corresponds to the inner region of a solar-type star protoplanetary disc. The initial pebble clump radius R_0 is 1500 km (that is $r_c = 1250$ km and $\sigma = 250$ km).

3.2. Grid and resolution

We perform 1D spherically symmetric simulations with a grid extending from $R_{\text{in}} = 0.0013R_0$ to $R_{\text{out}} = 4R_0$ or equivalently [2, 6000] km. The grid is uniform from 2 to 30 km and logarithmic from 30 to 6000 km giving a good balance between precision and numerical time. A grid comprising 2048 cells is considered, of which 306 are located in the uniform part from 2 to 30 km resulting in cells of 90 m. In the logarithmic part, the ratio between the grid spacing and position $\Delta x/x$ is approximately 0.003. This distribution of cells is designed such that the cell size in the uniform zone is comparable to the size of the first cell in the logarithmic zone. In order to circumvent the singularity at the centre and the considerable computational expense, the central zone between 0 and 2 km is not included in the simulation. Nevertheless, the mass of the gas and particles situated within this zone is represented by a central point mass, with the gravitational potential, designated as ϕ_c , being incorporated into the self-gravity potential in equations 5, 6 and 9.

3.3. Boundary conditions

At the outer edge, the outflow boundary condition is used with extrapolated primitive quantities. We performed tests with different boundary conditions and no apparent difference has been seen with zero gradient boundary conditions, showing that the size of the grid is chosen large enough to avoid such numerical artefacts.

At the inner edge, we use a no-inflow boundary condition. The density and pressure (for the gas) are copied from the innermost cell to the ghost zone (no gradient), the radial velocity is capped at 0 in ghost cells, and the mass flux is set to 0 in case of a positive flux entering the simulation grid. The mass lost at the inner edge is appended to the central point mass, thereby contributing to the overall dynamics of the system via the potential ϕ_c .

3.4. Test

To test the code and verify the compatibility of the different modules, we reproduced the results obtained by Shariff & Cuzzi (2015). The main difference in the approach is the numerical methods used to solve the hydrodynamic equations, and the boundary condition at the inner edge of the grid. Our approach shows good agreement with their results (as presented in appendix B.1), proving that we correctly capture the physics.

4. Numerical results of gravitational collapses

4.1. Fiducial run

Figure 2 shows radial profiles of the particle density and the evolution of the central gas density and temperature of our fiducial run. This reference run done with the Eulerian approach for the pebbles has a free fall time of $t_{\text{ff}} = 1.44 \times 10^6$ s. The coloured

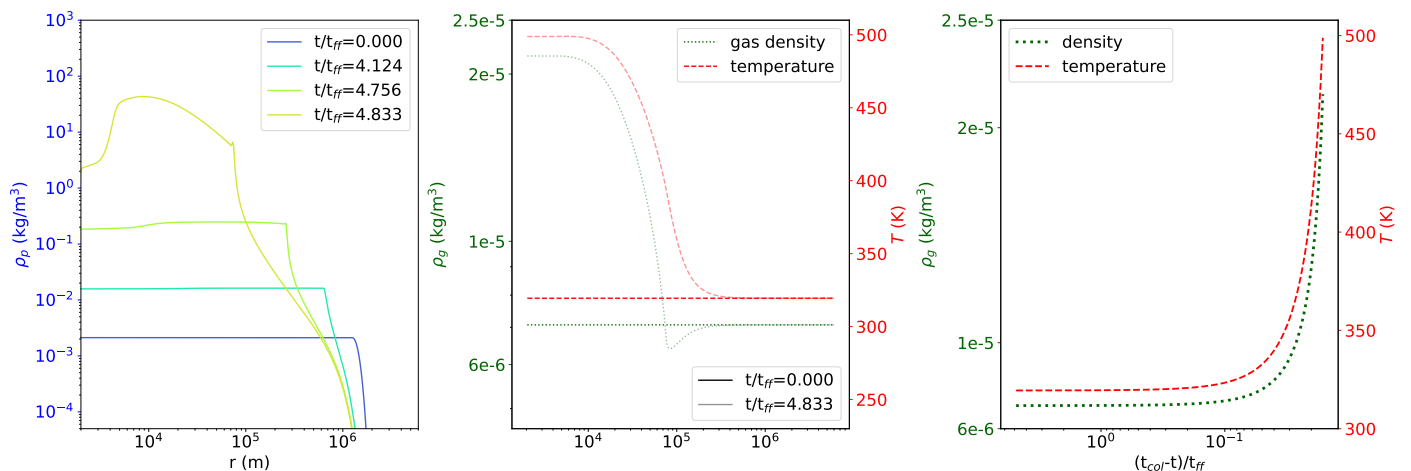


Fig. 2: (Left) Time evolution of the radial profile of the particle cloud density. (Centre) Gas temperature profiles (dashed) and gas density profiles (dotted), plotted at the beginning and the end of the fiducial run. (Right) Time evolution of the central density (dotted) and temperature (dashed, right axis) of the gas.

curves are traced for different times, that are characterized by the mean radius r_m of the pebble clump. This mean radius evolves from $0.5R_0$ at the beginning of the simulation to $0.02R_0$. This final mean radius corresponds to a core radius of 100 km. The collision time starts to be smaller than the friction time (see appendix A.2 for estimation of these times). The collisions not being included here, we do not follow further the collapse. The temperature plotted here (red dashed curves) is computed from the primitive variables, density (green dotted curves) and pressure, using the perfect gas law.

The radial density profile of the pebble cloud is shown on the left of Figure 2. The core of the cloud has a radially uniform density for most of the collapse but the concavity of the tail changes and the edge of the cloud becomes steep. Its value increases with time during the collapse, to reach $30 \text{ kg} \cdot \text{m}^{-3}$. However, this increase is not regular in time. The initial density is multiplied by 100 before $4.7t_{\text{ff}}$, and then multiplied by another factor of 300 at the end of the run, only $0.1t_{\text{ff}}$ later. We find the same behaviour for the gas density and temperature shown on the right plot. They are almost constant during the collapse up to $4.7t_{\text{ff}}$ (i.e. $(t_{\text{col}} - t)/t_{\text{ff}} \sim 10^{-1}$) and change only at the end of the collapse, with a final increase of the central density by a factor 3 and of the gas central temperature by about 170 K. The dashed red curves in the left panel correspond to the temperature profile at the beginning and the end of the collapse. It can be seen that the temperature evolution occurs only within the pebble cloud. In particular, the edge of the temperature rise zone and the edge of the pebble cloud overlap quite well. The increase in gas temperature of 170 K, small compared to the value estimated in section 2.3, also shows that the simple approach used there is not correct, as it assumes the pebble kinetic energy to be fully converted into gas heating. In fact, the kinetic energy represents indeed more than half of the released gravitational energy.

4.2. Heating processes

This section examines the heating that occurs during the fiducial run. Initially, the gas is a reservoir of gravitational energy with no kinetic energy, with two external sources of energy: the frictional heating of particles depositing their gravitational energy in the gas, and an energy transfer at the domain outer boundary. The latter would result in a temperature increase also at the

outer edge of the computational domain, which we do not see. The central heating is not an outer boundary effect. Therefore, to identify the origin of the gas heating in the fiducial run, we follow Huang & Bai (2022) and introduce a gas frictional heating parameter ω in equation 13

$$\mathcal{P}_{\text{drag}} = \rho_p \frac{\mathbf{v}_p - \mathbf{u}}{\tau_s} \cdot \mathbf{u} + \omega \rho_p \frac{(\mathbf{v}_p - \mathbf{u})^2}{\tau_s}. \quad (18)$$

ω ranges from 0 for no frictional heating of the gas (in other words this energy would heat the particles) to $\omega = 1$ corresponding to a full transfer of the energy dissipated through friction to gas thermal energy. We compare in Figure 3 the evolution of the central gas temperature during the contraction for two extreme cases $\omega = 1$ and $\omega = 10^{-3}$. The weak difference indicates that frictional heating is negligible compared to compressional heating, with a contribution of 1 K to the total temperature increase of about 170 K, as shown by the inset on Figure 3. As it will be discussed subsequently, this variation is of a similar magnitude to that introduced by modifying the resolution of our grid. Therefore, this is not a physically significant phenomenon. This shows that the heating of the gas is not due to the irreversible term of equation 13. We also note that the density minimum seen in Figure 2 is not present for weak frictional heating.

We now consider particle drag as a precursory process initiating the gas compression responsible for the temperature increase. We compare the gas temperature with the adiabatic evolution given by the Laplace law for perfect gas (dashed curve in Figure 3). The two curves perfectly overlap, showing that adiabatic heating is the main process responsible for the gas temperature increase at the centre of the cloud. To identify how the adiabatic compression occurs, we study in Figure 4 the radial profiles computed for the two extreme values of ω at the same run time. One can see that the density radial profiles (blue), and the central and outer temperature (red) perfectly match in the two runs. This is consistent with the irreversible term being negligible in the collapse dynamics. A temperature mismatch is seen only at the cloud rim that coincides with the region of non-negligible frictional heating ($\omega = 1$). The irreversible term of equation 13 has a non-negligible contribution only at the edge of the pebbles cloud. In this region, the temperature increase is higher for $\omega = 1$ than $\omega = 0.001$. Finally, the amplitude of the (negative) drag force that does not vary with ω , is maximum also at the cloud rim.

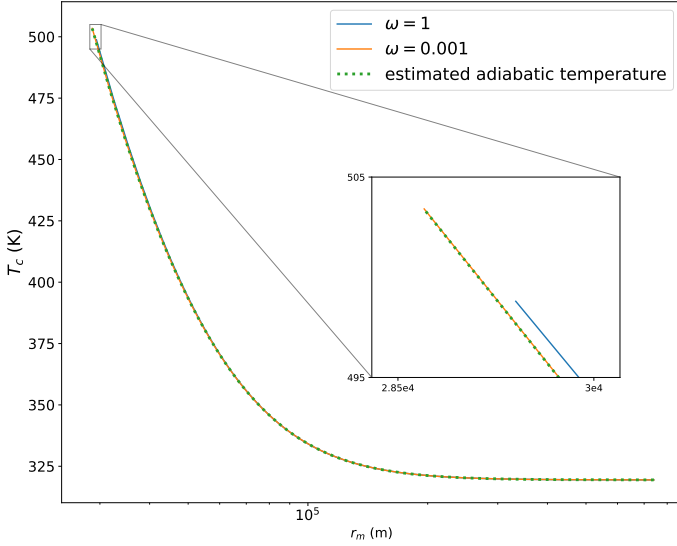


Fig. 3: Gas central temperature as a function of the cloud mean radius for two extreme values of ω . The dotted curve corresponds to the theoretical temperature for an adiabatic evolution.

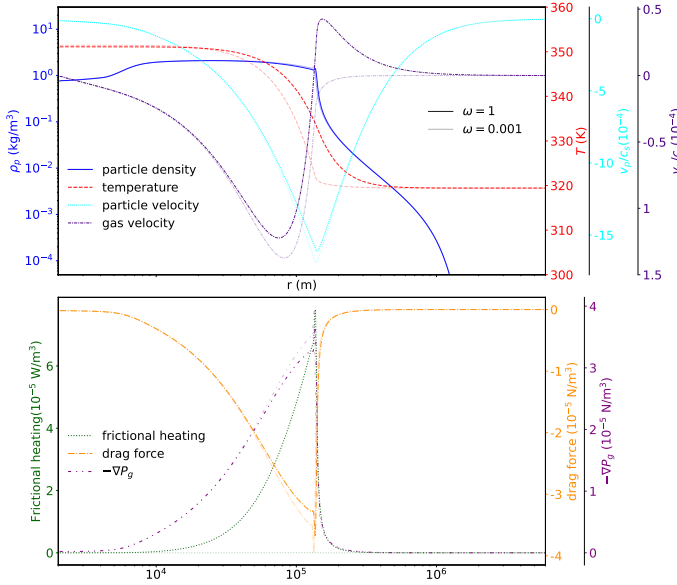


Fig. 4: Radial profiles of (top) pebble density (blue, left), gas temperature (red, right), pebble velocity (cyan, right), gas velocity (indigo, right), and (bottom) frictional heating (green, left), drag force (orange, right) and gas pressure gradient (violet, right) at $t/t_{ff} = 4.756$ for $\omega = 1$ (fiducial case) and $\omega = 0.001$

Indeed, most of the pebbles' momentum is at the cloud edge, so this layer dominates the work of the drag force transferred to the gas. Furthermore, one can see that the gas pressure gradient and the drag force are nearly opposite. Consequently, the pebble drag action on the gas can be conceptualized as a piston compressing and heating the inner gas in an adiabatic process.

4.3. Thermal exchanges between gas and pebbles.

In this section, we consider the thermal exchanges between the gas and the pebbles that were previously neglected. To include these thermal exchanges, we now also consider the time evolu-

tion of the specific internal energy of the pebbles u_d . It is advected with the flow of pebbles with velocity v_d and solves

$$\partial_t(\rho_d u_d) + \nabla \cdot (v_d \rho_d u_d) = S_d \quad (19)$$

S_d is the source term modelling representing the thermal energy transfer from the gas to the pebbles. It is therefore subtracted from the gas energy equation to ensure the energy conservation of the whole system.

A rigorous estimation of these thermal exchanges is complex and would need a precise understanding of the structure of the pebbles (size, shape, composition, porosity,...). We choose here to set S_d as a heat transfer at the surface of spherical pebbles and write (see e.g. Bird et al. 2006, equation 14.1.1)

$$S_d = h s (T_g - T_d) \quad (20)$$

In this equation, h is the heat transfer coefficient associated with the fluid and s is the exchange surface between gas and pebbles per fluid volume. h is computed from the gas thermal conductivity k (given by the kinetic theory of gases) and the size of pebbles a through the Nusselt number $Nu = \frac{ha}{k}$. We use the expression of the Nusselt number given by Bird et al. (2006, equation 14.4.5) $Nu = 2 + 0.6Re^{1/2}Pr^{1/3}$. For the flow considered in our simulation of a perfect gas around pebbles we have, $Re \ll 1$ and $Pr \sim 1$, so we will consider $Nu \approx 2$ and therefore $h = \frac{2k}{a}$. Moreover, s is given by $s = \frac{\rho_d}{4\pi\rho_m a^3/3} \times 4\pi a^2$ where the first term is the number density of pebbles and the second the surface of a pebble. Finally, T_g is the gas temperature and T_d is the temperature of the pebbles. The pebble temperature is related to the internal energy through the specific heat capacity of pebbles C_d . We consider the initial pebble temperature to be at the equilibrium with the gas and the internal energy is defined as the variation from the initial one. We therefore have

$$C_d(T_d - T_d(t=0)) = \underbrace{u_d}_{320 \text{ K}} - \underbrace{u_d(t=0)}_0 \quad (21)$$

Three values of C_d were considered to represent the efficiency of heat transfer through a pebble:

- C_d is given by the specific heat capacity of silicates C_{Si} ($\sim 900 \text{ J} \cdot \text{kg}^{-1} \cdot \text{K}^{-1}$). This means that the thermal diffusion inside a pebble is very efficient, and the temperature is uniform throughout the solid.
- $C_d = 0.01C_{Si}$: thermal diffusion is weakly efficient on timescales involved here and only 1% of pebbles heat.
- $C_d = 0.001C_{Si}$: thermal diffusion is poorly efficient and only the very surface of pebbles heats.

We also note that $C_d = 0$ corresponds to our previous simulations (no heating of the pebbles). With this approach, we obtain that the resulting surface temperature of the pebbles is very similar to the gas one. The increase in gas temperature at the inner edge of the simulation strongly varies with the specific heat capacity as shown in table 2. This is an expected result as the energy converted from the pebble velocity to internal energy is distributed into the gas and a mass of solids which strongly varies. Indeed at the end of the simulation, way before the end of the collapse, the pebble-to-gas ratio is already very high (of the order of $10^5 - 10^6$ as can be seen in figure 2) and the internal energy lies mostly in the pebbles.

This result questions how the total amount of internal energy that will be distributed between gas and solids, varies with the

case	ΔT_g
$C_d = 0$	175 K
$C_d = 0.001C_{Si}$	10.7 K
$C_d = 0.01C_{Si}$	1.6 K
$C_d = C_{Si}$	0.02 K

Table 2: Gas temperature increase depending on the strength of thermal exchanges between gas and pebbles.

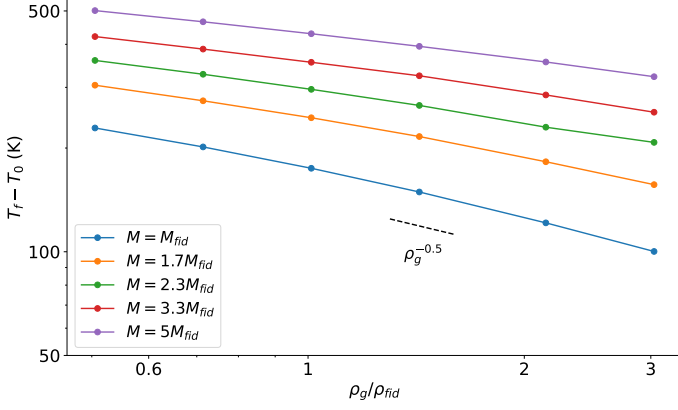


Fig. 5: Increase in gas central temperature as a function of the initial gas density, for different values of the initial mass of pebbles.

properties of the initial cloud. The thermal diffusion properties of the pebbles being unknown, we consider in the following this global internal energy of the system as represented by the gas temperature when the pebbles do not heat ($C_d = 0$).

4.4. Parameter exploration

4.4.1. Initial mass and density

We study how the final central gas temperature evolves with two parameters: the total mass of the pebble cloud M_{tot} and the initial gas density ρ_g , characterized by $M_{fid} = 3 \times 10^{16}$ kg and $\rho_{fid} = 7 \times 10^{-6}$ kg \cdot m $^{-3}$. As shown in Fig. 5, the final central temperature is approximately inversely proportional to the square root of the initial gas density. However, the slope of the curve varies slightly with the initial cloud mass. To better characterize this behaviour, the final temperature is plotted as a function of the initial mass in Fig. 6. The final temperature is nearly proportional to the initial mass, but again, with a slight dependence on the gas density.

These behaviours are consistent with what we might expect: the more massive the pebble clump, the more energy is released, and the higher the temperature of the gas surrounding the forming planetesimal. Similarly, if there is less gas surrounding the clump, the gas will be hotter, for the same amount of energy released. These results show that, to dissolve gas from the disc into the forming planetesimal (i.e. to reach a temperature of about 1200 K), a massive clump (mass of about 10^{17} kg, corresponding to a planetesimal of about 20 km in size) with a low surrounding gas density (initial dust-to-gas ratio of about 1000 or more) is required, as well as a nearly-zero thermal diffusion in the pebbles.

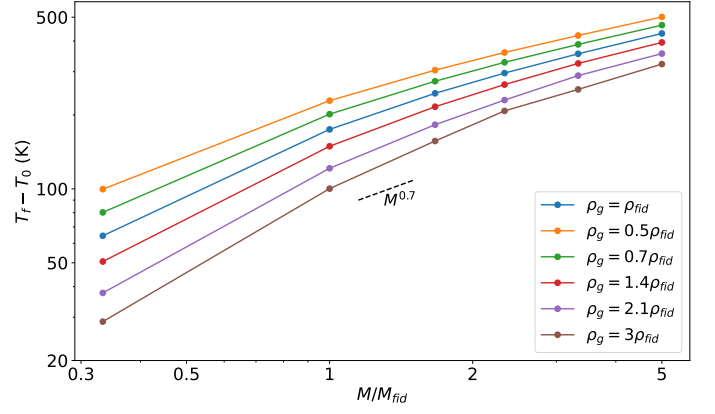


Fig. 6: Increase in the gas central temperature as a function of the initial mass of pebbles for different values of initial gas density.

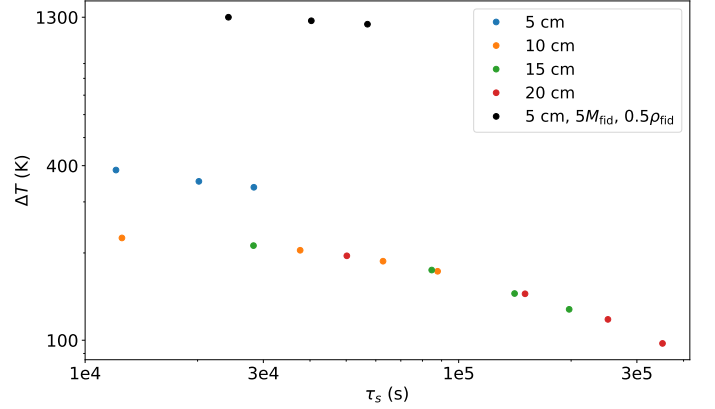


Fig. 7: Gas central temperature increase as a function of the initial stopping time of pebbles.

4.4.2. Size and intrinsic density of pebbles

We also study the influence of the coupling between gas and particle by varying the initial stopping time of the pebbles. This was made by modifying either the size or the internal density of the pebbles. Sizes were chosen between 5 and 20 cm and densities between 1 and 7 g \cdot cm $^{-3}$ (pebbles made of different materials from ice to iron depending on porosity). Because of the transition in the formulation of the stopping time between the Epstein and Stokes drag law for $s = 6.9$ cm in our fiducial setup where the mean free path of the gas is $\lambda = 2.9$ cm, there is a dichotomy in behaviour between the 5 cm pebbles and the others. If we first consider the solids larger than 10 cm, one can see in figure 7 that the smaller the initial stopping time, the hotter the gas at the end of the run. Indeed, the drag term in equations 5 and 6 is inversely proportional to the stopping time. Thus, for smaller and less dense pebbles, more coupled to the gas, the piston effect is more efficient and the gas temperature is higher. This correlation between the stopping time and adiabatic heating is also responsible for the dichotomy seen in Fig. 7 between the 5 cm size pebbles and the other, for the same initial stopping time. Indeed in a perfect gas, the mean free path λ is proportional to ρ_g^{-1} . Therefore, with eq. 12, we have $\tau_s \propto (\rho_g \bar{c})^{-1}$ for Epstein law and $\tau_s \propto \bar{c}^{-1}$ for Stokes law. It implies that for a fixed-size solid the modification of its stopping time with the gas density and temperature is larger in the Epstein regime. Thus, for two pebbles with the same initial stopping time, the one in the Epstein regime

will become more coupled to the gas as the collapse progresses than the one in the Stokes regime. So, at the end of the simulation, the piston effect will be more efficient for small pebbles than for big ones.

Figures 5, 6 and 7 demonstrate that the maximum temperature increase in the gas is achieved when the initial gas density is the lowest, the total mass of the cloud is the largest or the pebbles are the smallest. In the parameter range under consideration (see Table 1), the greatest temperature increase is therefore observed for $M_{tot} = 5M_{fid}$, $\rho_g = 0.5\rho_{fid}$ and $a = 5$ cm. We run the corresponding simulations, whose result corresponds to the black dots in figure 7. In this case, we obtain an increase of about 1300 K resulting in a final temperature of approximately 1600 K.

5. Discussion and Conclusion

To ascertain the impact of numerical resolution on the results, additional simulations were conducted using the same initial conditions as the fiducial case but with an increasing number of cells. The findings are presented in appendix B.2. We verify that increasing the resolution does not change the physical results, whereas decreasing it could occasionally result in minor numerical instabilities.

The previous exploration of the parameter space shows the importance of the gas heating process during planetesimal formation by gravitational collapse. However, due to the simplicity of our approach, there are several limitations.

First, the collapse is assumed to be spherically symmetric. This implies that convection in the gas, as well as rotation, are neglected. In our fiducial simulation, we estimated the Brunt–Väisälä frequency, designated as N . It was found that the value of N^2 is positive in the edge zone at a radius $r \approx 10^5$ km. However, the value of N is $\approx 10^{-4}$ Hz resulting in a characteristic time of 10^4 s. This timescale is however of the order of the temperature evolution timescale, casting doubts on the viability of genuine convection. So, the temperature profiles shown in Figure 2 reached at the end of the simulation might be prone to convection. However, this estimation is made without any cooling. This process would imply a redistribution of energy within the gas, which would reduce the final central temperature.

Finally, we do not consider particle collisions, despite their potentially key role in planetesimal formation (Nesvorný et al. 2010, 2021; Wahlberg Jansson et al. 2017; Wahlberg Jansson & Johansen 2017; Polak & Klahr 2023) for two reasons. First, we run 1D simulations, with no initial velocity dispersion, making collisions meaningless here. Second, unlike Nesvorný et al. (2010, 2021) who focus on Kuiper belt objects, we consider planetesimal formation closer to 1 AU with denser and hotter gas, leading to stronger friction, which may dominate the effect of collisions in the first phase of the collapse (see a comparison between stopping time and collision time in appendix A.2). It is a reasonable assumption that collisions will play a crucial role in the subsequent evolution. This is due to the fact that collisions will facilitate a conversion of the kinetic energy of the pebbles into internal energy, which will in turn influence the temperature of the pebbles.

To conclude, in this paper, we have extended the Shariff & Cuzzi (2015) approach of the gravitational collapse of a gas and pebble cloud, by considering the gas thermodynamics. We first show an increase in the collapse time of the pebble cloud due to the gas friction. This increase is inversely proportional to the Stokes number $St_{ff} = 2\pi\tau_s/t_{ff}$. Secondly, we have provided evidence that the heating of the gas at the centre of the domain is caused by gas adiabatic compression driven by the pebbles

dragging the gas with them as they collapse. Three regions can be identified as associated with different heating. In the outermost region without particles, there is no temperature increase. Frictional heating, when present, heats only the particle cloud rim. The temperature rise in the core of the cloud is dominated by adiabatic compression driven by the deposition of momentum in the rim. We also show how this heating varies with the clump mass, the gas density and the characteristics of the pebbles. In the most massive clumps, more gravitational energy will be released during the collapse, and thus the pebbles will reach a higher velocity. Moreover, if these clumps are made of small pebbles, the coupling between pebbles and gas is stronger, which implies that the piston effect is more efficient. Therefore in these clumps, the gas might reach the temperature needed for dissolution into the forming planetesimal. Furthermore, the final stages of the collapse are not modelled in this study. If the collapse were to be simulated to a greater extent, a higher temperature should be reached. The temperature might be high enough (up to about 1500 K) for the pebbles to experience thermal metamorphism, and, maybe, even a melting favouring a gas dissolution into it, or degassing of trapped gases. However, these results depend strongly on the thermal exchanges between gas and pebbles and on their composition. At such pebble scales, geochemical experiments of gas dissolution into silicates show that this process could be highly effective in a few hours (see e.g. Jambon et al. 1986). This work demonstrates that the melting of the pebble surface might be obtained during the gravitational collapse over a timescale of 10^{-2} free-fall time (5 hours here) in favourable conditions (massive clump, small pebbles, low to nearly zero thermal diffusion). Therefore even for planetesimals small compared to the characteristic size of parent bodies of the current main belt asteroids, the temperature increase might be consistent with a gas dissolution in the planetesimal-forming pebbles. However, one should note that the cooling process after the planetesimal formation is not considered here.

These results emphasize the key role of the gas in the formation of planetesimals with gravitational collapse, especially at distances of a few AUs from the central star. This implies a new step in the thermal history of planetesimals depending strongly on their formation region. The identified heating process may lead to local heating not only in space but also in time which could provide new approaches for cosmochemical studies. This work also suggests future avenues for studying the gravitational collapse of a pebble clump in a gaseous environment: first, by extending the simulations to 2D or 3D, opening up the possibility of including initial particle velocity dispersion and collisions, and second, by better modelling the thermal exchange between pebbles and gas.

Acknowledgements. This work was supported by the French government through the France 2030 investment plan managed by the National Research Agency (ANR), as part of the Initiative of Excellence Université Côte d’Azur under reference number ANR-15-IDEX-01. The authors are grateful to the Université Côte d’Azur’s Center for High-Performance Computing (OPAL infrastructure) for providing resources and support. It has received support from the CNRS Origines and ‘Programme national de Planétologie’ (PNP). The authors would like to thank the anonymous referee for the very useful comments that helped to improve greatly this paper.

References

- Bird, R., Stewart, W., & Lightfoot, E. 2006, *Transport Phenomena* (Wiley)
- Blum, J. 2018, *Space Sci. Rev.*, 214, 52
- Boyet, M., Bouvier, A., Frossard, P., et al. 2018, *Earth Planet Sci. Lett.*, 488, 68
- Carrera, D. & Simon, J. B. 2022, *ApJL*, 933, L10
- Cuzzi, J. N., Hogan, R. C., Paque, J. M., & Dobrovolskis, A. R. 2001, *ApJ*, 546, 496

- Dittrich, K., Klahr, H., & Johansen, A. 2013, *ApJ*, 763, 117
- Epstein, P. S. 1924, *Phys. Rev.*, 23, 710
- Fromang, S. & Nelson, R. P. 2006, *A&A*, 457, 343
- Gerosa, F. A., Méheut, H., & Bec, J. 2023, *Eur. Phys. J. Plus*, 138, 9
- Gratton, R., Ligi, R., Sissa, E., et al. 2019, *A&A*, 623, A140
- Hasegawa, Y., Suzuki, T. K., Tanaka, H., Kobayashi, H., & Wada, K. 2021, *ApJ*, 915, 22
- Hasegawa, Y., Suzuki, T. K., Tanaka, H., Kobayashi, H., & Wada, K. 2023, *ApJ*, 944, 38
- Hayashi, C. 1981, *Prog. Theor. Phys. Supp.*, 70, 35
- Huang, P. & Bai, X.-N. 2022, *ApJS*, 262, 11
- Jambon, A., Weber, H., & Braun, O. 1986, *Geochim. Cosmochim. Acta*, 50, 401
- Johansen, A., Klahr, H., & Henning, T. 2011, *A&A*, 529, A62
- Johansen, A. & Lambrechts, M. 2017, *Annu. Rev. Earth Planet. Sci.*, 45, 359
- Keppeler, M., Benisty, M., Müller, A., et al. 2018, *A&A*, 617, A44
- Klahr, H. & Hubbard, A. 2014, *ApJ*, 788, 21
- Kobayashi, H. & Tanaka, H. 2021, *ApJ*, 922, 16
- Kobayashi, H. & Tanaka, H. 2023, *ApJ*, 954, 158
- Krapp, L., Benítez-Llambay, P., Gressel, O., & Pessah, M. E. 2019, *ApJL*, 878, L30
- Kruijjer, T. S., Touboul, M., Fischer-Gödde, M., et al. 2014, *Science*, 344, 1150
- Lesur, G., Flock, M., Ercolano, B., et al. 2023, in *Astronomical Society of the Pacific Conference Series*, Vol. 534, *Protostars and Planets VII*, ed. S. Inutsuka, Y. Aikawa, T. Muto, K. Tomida, & M. Tamura, 465
- Lesur, G. R. J., Baghdadi, S., Wafflard-Fernandez, G., et al. 2023, *A&A*, 677, A9
- Lichtenberg, T., Schaefer, L. K., Nakajima, M., & Fischer, R. A. 2023, in *Astronomical Society of the Pacific Conference Series*, Vol. 534, *Protostars and Planets VII*, ed. S. Inutsuka, Y. Aikawa, T. Muto, K. Tomida, & M. Tamura, 907
- Lorek, S. & Johansen, A. 2024, *A&A*, 683, A38
- Lovelace, R. V. E., Li, H., Colgate, S. A., & Nelson, A. F. 1999, *ApJ*, 513, 805
- Lyra, W. 2014, *ApJ*, 789, 77
- Manger, N. & Klahr, H. 2018, *MNRAS*, 480, 2125
- Mauxion, J., Lesur, G., & Maret, S. 2024, *A&A*, 686, A253
- Meheut, H., Meliani, Z., Varniere, P., & Benz, W. 2012, *A&A*, 545, A134
- Mignone, A., Bodo, G., Vaidya, B., & Mattia, G. 2018, *ApJ*, 859, 13
- Morbidelli, A. & Nesvorný, D. 2020, in *The Trans-Neptunian Solar System*, ed. D. Prrialnik, M. A. Barucci, & L. A. Young (Elsevier), 25–59
- Nelson, R. P., Gressel, O., & Umurhan, O. M. 2013, *MNRAS*, 435, 2610
- Nesvorný, D., Li, R., Simon, J. B., et al. 2021, *Planet. Sci. J.*, 2, 27
- Nesvorný, D., Youdin, A. N., & Richardson, D. C. 2010, *AJ*, 140, 785
- Pan, L., Padoan, P., Scalo, J., Kritsuk, A. G., & Norman, M. L. 2011, *ApJ*, 740, 6
- Polak, B. & Klahr, H. 2023, *ApJ*, 943, 125
- Raettig, N., Lyra, W., & Klahr, H. 2021, *ApJ*, 913, 92
- Schaffer, N., Johansen, A., & Lambrechts, M. 2021, *A&A*, 653, A14
- Shariff, K. & Cuzzi, J. N. 2015, *ApJ*, 805, 42
- Urpín, V. & Brandenburg, A. 1998, *MNRAS*, 294, 399
- Wahlberg Jansson, K. & Johansen, A. 2017, *MNRAS*, 469, S149
- Wahlberg Jansson, K., Johansen, A., Syed, M. B., & Blum, J. 2017, *ApJ*, 835, 109
- Weidenschilling, S. J. 1977, *MNRAS*, 180, 57
- Youdin, A. N. & Goodman, J. 2005, *ApJ*, 620, 459
- Zhu, K., Schiller, M., Moynier, F., et al. 2023, *Geochim. Cosmochim. Acta*, 342, 156

Appendix A: Derivation of analytic formulas

Appendix A.1: Free-fall time

The free-fall time of a particle clump can be calculated using the same reasoning as in section 2.1. The position of a free-falling particle at the cloud edge solves

$$\frac{d^2 r}{dt^2} = -\frac{\mathcal{G}M}{r^2} \quad (\text{A.1})$$

This equation can be integrated for a static initial condition and an initial radius R_0 giving

$$\frac{dr}{dt} = -\sqrt{2\mathcal{G}M\left(\frac{1}{r} - \frac{1}{R_0}\right)}, \text{ and} \quad (\text{A.2})$$

$$t = \sqrt{\frac{R_0^3}{2\mathcal{G}M}} \left(\sqrt{x(1-x)} + \arcsin(\sqrt{1-x}) \right), \quad (\text{A.3})$$

where $x = r/R_0$. The free-fall time corresponds to the time where r (or x) reaches 0, which gives

$$t_{\text{ff}} = \frac{\pi}{2} \sqrt{\frac{R_0^3}{2\mathcal{G}M}} \quad (\text{A.4})$$

Appendix A.2: Comparison of collision time versus stopping time

Building on Nesvorný et al. (2010), we compare the stopping time and the time between pebble collisions. The stopping time is estimated in the Epstein regime as $\tau_s = \rho_m a / \rho \bar{c}$ with the notations defined in section 2.2. The collision time is given by $\tau_c \sim (n\sigma v)^{-1}$, with the pebbles number density $n \sim M_{\text{tot}} / (\rho_m a^3 R^3)$, the cross-section $\sigma \sim a^2$, and the virial velocity $v \sim \sqrt{\mathcal{G}M_{\text{tot}}/R}$. Bringing all together leads to

$$\frac{\tau_s}{\tau_c} \sim \sqrt{\frac{\mathcal{G}M_{\text{tot}}^3}{\rho^2 \bar{c}^2 R^7}}. \quad (\text{A.5})$$

With the values for M_{tot} , ρ , \bar{c} and R used in our fiducial simulation, we have $\tau_s/\tau_c \sim 1$. Thus, the stopping time and the collapse time are approximately the same in this situation and thus the friction due to the gas can not be neglected. However, we have here $v \sim 1 \text{ m} \cdot \text{s}^{-1}$ which is an order of magnitude higher than the typical velocity observed in our simulation (a so high velocity is obtained only at the end of the collapse). We can then consider that for our simulations, $\tau_s \ll \tau_c$ so that the friction is dominant for the major part of the collapse.

Appendix B: Test of the numerical setup

Appendix B.1: Comparison with previous work

To test our numerical setup we provide here a comparison with the work of Shariff & Cuzzi (2015) where they use a similar approach for the modelisation of the system but with different numerical methods to solve hydrodynamics and Poisson equations. Moreover, we test the lagrangian particle module of IDEFIX, as the dynamic of the pebbles is this time solved very differently.

The notations used here are the same as section 4.1 of Shariff & Cuzzi (2015). J_t corresponds to a two-phase Jeans number which compares the propagation time of a sound wave across the

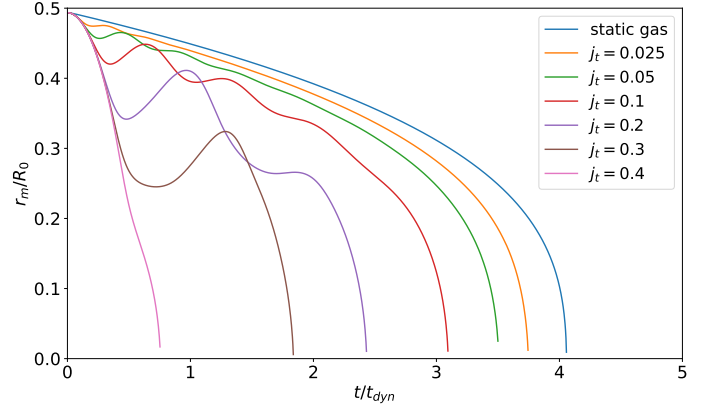


Fig. B.1: Size evolution of the particle cloud for various J_t ($\text{St}_{\text{ff}} = 0.02$, $\phi_0 = 100$) with our Eulerian approach for pebbles

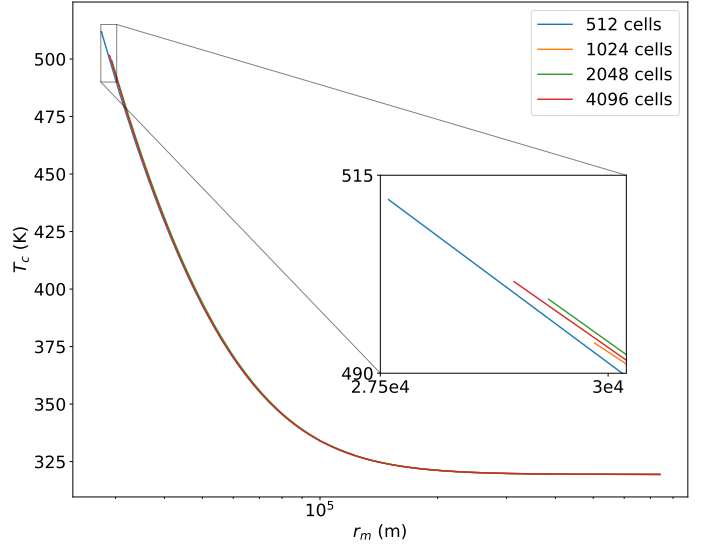


Fig. B.2: Evolution of the gas central temperature with the cloud mean radius for different numerical refinements.

clump with the dynamical time $t_{\text{dyn}} = (\rho_p \mathcal{G})^{-1/2} = \sqrt{32/3\pi} t_{\text{ff}}$. Figure B.1 compares the size evolution of the clump for various J_t and should be compared with Figure 3 of Shariff & Cuzzi (2015). We obtain results similar to the original study, which justifies our methodological approach to the problem.

Appendix B.2: Convergence test

We run our fiducial run for different resolutions, from 512 to 4096 cells. The results are shown in Figures B.2 and B.3. We see that increasing the resolution does not change the physical results (small variation of about 2 K, which is 1% of the temperature increase at the end of the collapse). However, we see that at low resolution there are some numerical instabilities at the edge of the cloud. We therefore decide to use a resolution of 2048 cells as a compromise between these instabilities and the simulation time.

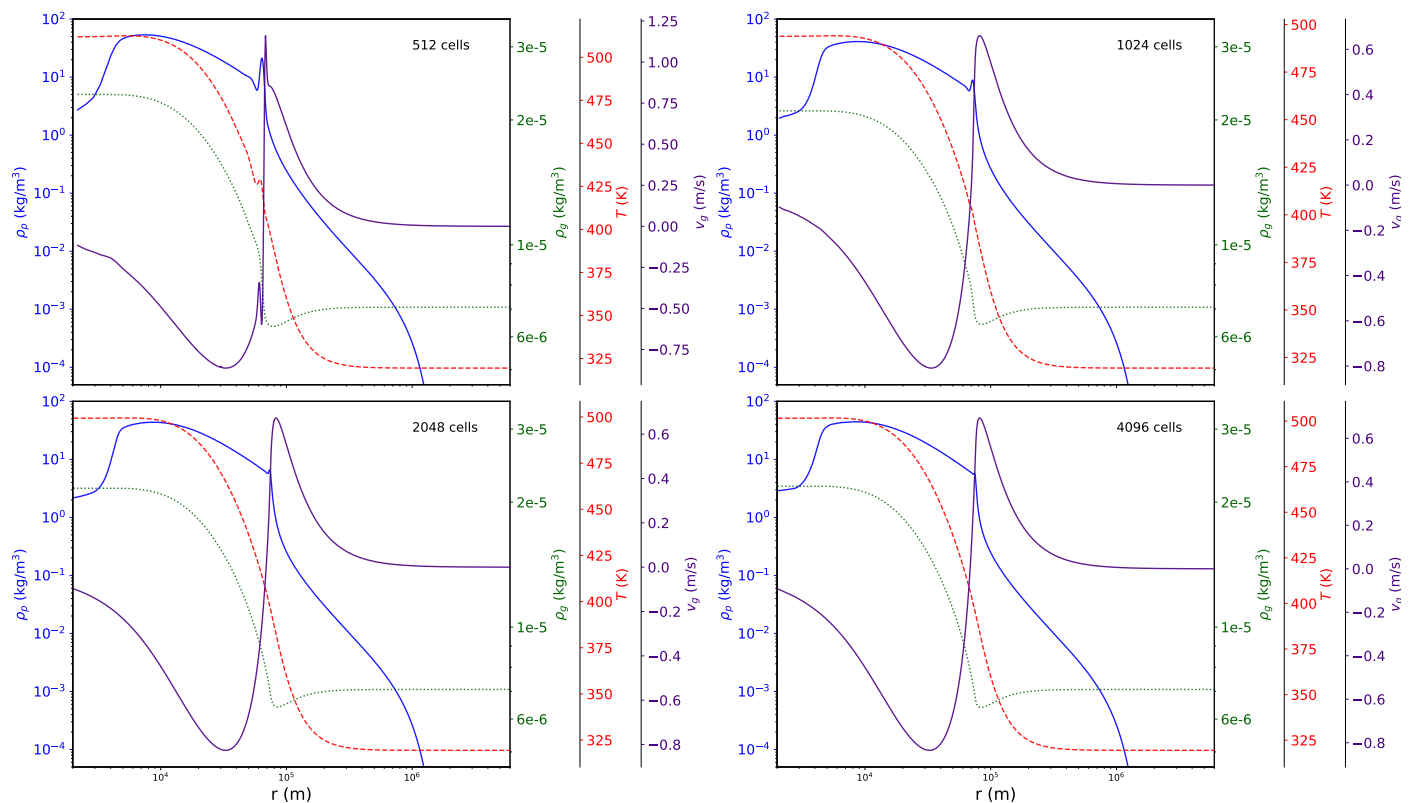


Fig. B.3: Radial profiles of pebble density (blue), gas density (green), gas temperature (red), and gas velocity (indigo) at the end of the fiducial simulation ($t/t_{ff} = 4.756$) for different numerical refinement.

Appendix C: Lagrangian Particle approach

Two principal methods are typically employed to model the dynamical evolution of solids in gaseous proto-planetary discs. The first is the pressure-less fluid model, which is the focus of this paper. The second method is the Lagrangian particle approach, which involves the modelling of solids through a relatively small number of particles (referred to as super-particles, or SP). Each SP represents a large number of pebbles sharing the same properties, including size, internal density, velocity. The IDEFIX code enables the utilisation of these two approaches, and thus a comparison was undertaken. The principal characteristics of the Lagrangian particles module of the IDEFIX code are presented here, with a more comprehensive account to follow in a dedicated publication.

The SP follow the Newton equation:

$$\frac{d^2 \mathbf{x}_p}{dt^2} = -\nabla(\phi_{g+p}) - \frac{\mathbf{v}_p - \mathbf{u}}{\tau_s} \quad (\text{C.1})$$

where \mathbf{x}_p and \mathbf{v}_p are the position and the velocity of a SP. In order to compute the self-gravity and friction forces, the deposition of SP on the grid is carried out using a triangular shape cloud (TSC) scheme, as described by Mignone et al. (2018).

The simulation of the collapse employs the identical initial conditions and grid as the pressure-less fluid approach, with a single minor alteration. To reduce the computational time, an evolving mesh refinement is implemented. The simulation is conducted in three stages, corresponding to the intervals $[0.5, 0.15]R_0$, $[0.15, 0.05]R_0$, and $[0.05, 0.02]R_0$. At each restart, the resolution is increased from 1024 to 2048 and 4096 cells. This results in a reduction in the requirement for computational resources during the initial phase of the evolution process, while

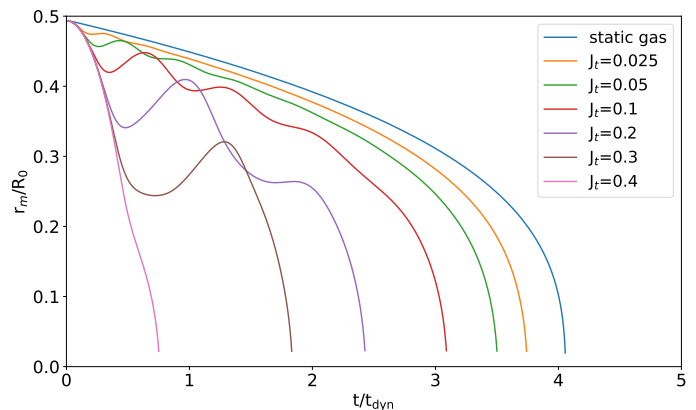


Fig. C.1: Size evolution of the particle cloud for various J_t ($St_{ff} = 0.02$, $\phi_0 = 100$) with a Lagrangian approach for pebbles

simultaneously enabling high precision during the accelerated evolution phase at the late stages of the collapse. In order to ensure continuity in cell size between the uniform zone and the logarithmic zone of the grid, the cells are distributed between the two zones in the same way as the simulations conducted with the pressure-less fluid approach. In order to achieve a smooth transition between two different steps, the final profiles from one step are used as the initial conditions for the subsequent step. These profiles, which relate to position, velocity and pressure (for the gas), are linearly interpolated on the new grid. In order to obtain sufficient resolution to correctly map the particle density onto the grid, each step is initialised with 10 particles per cell. We verified that there were no physical differences if we did only one step

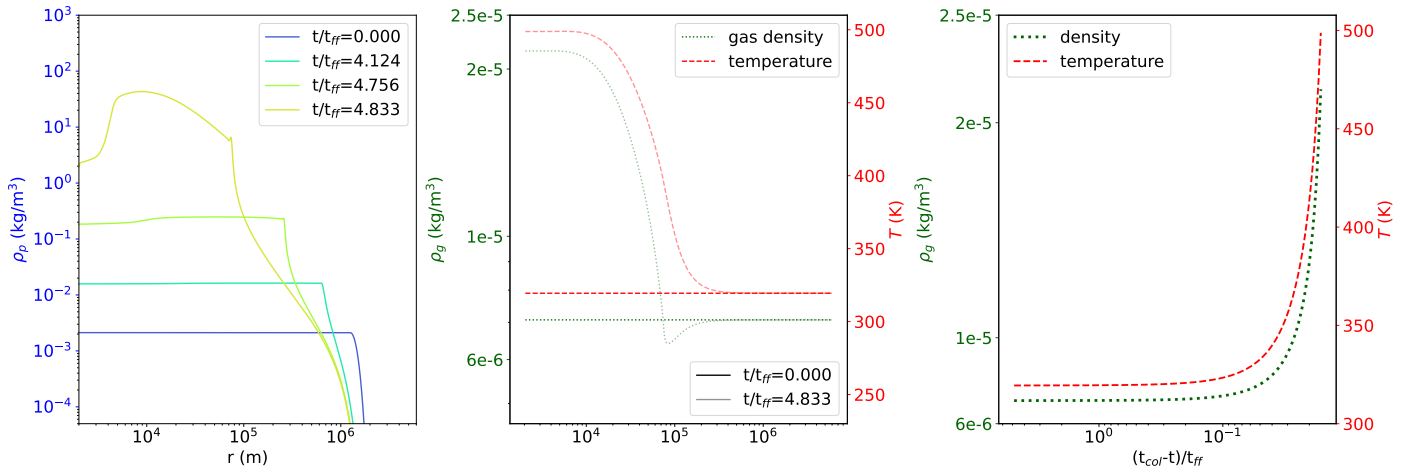


Fig. C.2: (Left) Time evolution of the radial profile of the particle cloud density. (Centre) Gas temperature profiles (dashed) and gas density profiles (dotted), plotted at the beginning and the end of the fiducial run. (Right) Time evolution of the central density (dotted) and temperature (dashed, right axis) of the gas.

with 2048 or 4096 cells. We use open boundary conditions, allowing SP to escape the grid, thereby precluding any possibility of re-entry. In a manner analogous to the pressure-less approach, the mass lost at the inner boundary is added to the central mass thereby contributing to ϕ_c .

Figure C.1 is the same as figure B.1, and figure C.2 is the same as figure 2 but for the Lagrangian particle approach. The results obtained are highly comparable, indicating that both methodological approaches are viable for modelling the collapse. The methodological choice will therefore be contingent upon the additional physical effects one wishes to consider, such as collisions or size distributions.